A population of faint low surface brightness galaxies in the Perseus cluster core

Carolin Wittmann,[1][*] Thorsten Lisker,[1] Liyualem Ambachew Tilahun,[1]
Eva K. Grebel,[1] Christopher J. Conselice,[2] Samantha Penny,[3] Joachim Janz,[4]
John S. Gallagher III,[5] Ralf Kotulla[5] and James McCormac[6,7]

[1]*Astronomisches Rechen-Institut, Zentrum für Astronomie der Universität Heidelberg, Mönchhofstraße 12-14, 69120 Heidelberg, Germany*
[2]*School of Physics and Astronomy, University of Nottingham, Nottingham, NG7 2RD, UK*
[3]*Institute of Cosmology and Gravitation, University of Portsmouth, Dennis Sciama Building, Burnaby Road, Portsmouth PO1 3FX, UK*
[4]*Centre for Astrophysics and Supercomputing, Swinburne University, Hawthorn, VIC 3122, Australia*
[5]*Department of Astronomy, University of Wisconsin at Madison, 475 North Charter Street, Madison, WI 53706-1582, USA*
[6]*Department of Physics, University of Warwick, Coventry CV4 7AL, UK*
[7]*Isaac Newton Group of Telescopes, Apartado de correos 321 , E-38700 Santa Cruz de La Palma, Canary Islands, Spain*

ABSTRACT

We present the detection of 89 low surface brightness (LSB), and thus low stellar density galaxy candidates in the Perseus cluster core, of the kind named 'ultra-diffuse galaxies', with mean effective V-band surface brightnesses 24.8-27.1 $\mathrm{mag\,arcsec^{-2}}$, total V-band magnitudes -11.8 to $-15.5\,\mathrm{mag}$, and half-light radii 0.7-4.1 kpc. The candidates have been identified in a deep mosaic covering 0.3 square degrees, based on wide-field imaging data obtained with the William Herschel Telescope. We find that the LSB galaxy population is depleted in the cluster centre and only very few LSB candidates have half-light radii larger than 3 kpc. This appears consistent with an estimate of their tidal radius, which does not reach beyond the stellar extent even if we assume a high dark matter content (M/L = 100). In fact, three of our candidates seem to be associated with tidal streams, which points to their current disruption. Given that published data on faint LSB candidates in the Coma cluster – with its comparable central density to Perseus – show the same dearth of large objects in the core region, we conclude that these cannot survive the strong tides in the centres of massive clusters.

Key words: galaxies: dwarf – galaxies: clusters: individual: Perseus – galaxies: photometry – galaxies: fundamental parameters – galaxies: evolution

1 INTRODUCTION

Galaxies of low surface brightness, once considered a rare part of the overall galaxy population (e.g., van den Bergh 1959), now are recognized to exist in all galaxy mass ranges with a wide variety of properties (e.g., Sprayberry et al. 1995; de Blok et al. 1996; Schombert et al. 2011; Boissier et al. 2016). In addition improved techniques have led to the detection of increasing numbers of low surface brightness, and thus low stellar density, galaxies (Impey et al. 1996; Dalcanton et al. 1997; Kniazev et al. 2004). These are particularly numerous among the less luminous members of galaxy clusters (e.g., van der Burg et al. 2016).

Galaxy clusters have been and are being surveyed for increasingly faint galaxies, leading to the detection of low mass dwarf galaxies in the surface brightness regime of Local Group dwarf spheroidals (dSphs) with mean effective surface brightnesses $\langle\mu_V\rangle_{50} > 24\,\mathrm{mag\ arcsec^{-2}}$, and even ultra-faint dwarfs (e.g. Muñoz et al. 2015; Ferrarese et al. 2016). With this increasing coverage of the parameter space of magnitude, half-light radius and surface brightness, we therefore consider it necessary to distinguish between a regular – even though faint – dwarf galaxy, and a low surface brightness (LSB) galaxy *in the sense of having a surface brightness clearly lower than average at its luminosity*. For example, while the Virgo Cluster Catalogue of Binggeli et al. (1985) contains hundreds of newly identified dwarf galaxies, many of them being faint in magnitude and surface brightness, their catalogue also includes a handful of LSB objects that seemed to form 'a new type of very large diameter (10 000 pc), low central surface brightness ($\geq$ 25 B $\mathrm{mag\,arcsec^{-2}}$) galaxy, that comes in both early (i.e., dE) and late (i.e., Im V) types' (Sandage & Binggeli 1984). Fur-

[*] E-mail: carolin@dwarfgalaxies.net

ther Virgo cluster galaxies of dwarf stellar mass but with unusually large size and faint surface brightness were described by Impey et al. (1988), and some similar objects were discovered in the Fornax cluster by Ferguson & Sandage (1988) and Bothun et al. (1991). Three decades later, galaxies in the same general parameter range were dubbed 'ultra-diffuse galaxies' by van Dokkum et al. (2015a).

In the Coma cluster, a large number of over 700 very faint candidate member galaxies with total magnitudes $M_B > -13$ mag, half-light radii $0.2 < r_{50} < 0.7$ kpc and central surface brightnesses as low as $\mu_{B,0} = 27$ mag arcsec^{-2} were identified by Adami et al. (2006). In the brighter and overlapping magnitude range $-11 \gtrsim M_g \gtrsim -16$ mag van Dokkum et al. (2015a) and Koda et al. (2015) reported numerous LSB candidates with $\mu_{g,0} \geq 24$ mag arcsec^{-2} and half-light radii up to 5 kpc in Coma, of which five large objects with $r_{50} \gtrsim 3$ kpc are spectroscopically confirmed cluster members (van Dokkum et al. 2015b; Kadowaki et al. 2017). The Virgo cluster study of Mihos et al. (2015, 2017) revealed four LSB candidates with even lower central surface brightnesses of $\mu_{V,0} \sim 27$ mag arcsec^{-2} and half-light radii as large as 10 kpc. In the Fornax cluster an abundant population of faint LSB galaxies with $\mu_{r,0} \geq 23$ mag arcsec^{-2} were catalogued by Muñoz et al. (2015) and Venhola et al. (2017), of which a few have $r_{50} > 3$ kpc (Venhola et al. 2017). Several such objects in different environments were also reported by Dunn (2010).

Although LSB galaxies have now been detected in large numbers, their origin remains a puzzle. Especially the abundant existence of LSB galaxies of dwarf stellar mass in galaxy clusters raised the question how these low stellar density systems could survive in the tidal field of such dense environments. For example, van Dokkum et al. (2015a) did not report any signs of distortions for the faint LSB candidates identified in the Coma cluster. Other cluster LSB galaxies of dwarf luminosity harbour surprisingly large and intact globular cluster (GC) systems (e.g. Beasley & Trujillo 2016; Peng & Lim 2016). One explanation could be that these galaxies are characterized by a very high dark matter content that prevents disruption of their stellar component. A similar interpretation was given by Penny et al. (2009) for a population of remarkably round and undistorted dSphs in the Perseus cluster core. Dynamical analyses of two faint LSB galaxies in the Coma and Virgo cluster indeed revealed very high mass-to-light ratios on the order of $M/L = 50 - 100$ within one half-light radius (van Dokkum et al. 2016; Beasley et al. 2016). Similar or even higher M/L ratios are also characteristic for Local Group dSphs with $M_V > -10$ mag or $\langle\mu_V\rangle_{50} > 25$ mag arcsec^{-2} (cf. McConnachie 2012). On the other hand Milgrom (2015) suggested that within the MOND theory high M/L ratios could also be explained if the LSB galaxies would contain yet undetected cluster baryonic dark matter.

However, apparently the above does not apply to all faint cluster LSB galaxies. For example two LSB galaxy candidates of very low stellar density in the Virgo cluster show possible signs of disruption (Mihos et al. 2015, 2017). One large LSB candidate of dwarf luminosity with a very elongated shape and truncated light profile was also reported in Fornax (Lisker et al. 2017), and several further elongated large LSB candidates were described by Venhola et al. (2017). In the Hydra I galaxy cluster Koch et al. (2012) iden-

tified a faint LSB galaxy with S-shaped morphology, indicative of its ongoing tidal disruption. Also van der Burg et al. (2016), who studied populations of faint LSB candidates with $r_{50} \geq 1.5$ kpc in eight clusters with redshifts z = $0.044 - 0.063$, reported a depletion of LSB galaxy candidates in the cluster cores, based on number counts. Similarly, the numerical simulations of Yozin & Bekki (2015) predict the disruption of LSB galaxies that are on orbits with very close cluster-centric passages.

In this study we aim to investigate the faint LSB galaxy population of the Perseus cluster core. Perseus is a rich galaxy cluster at a redshift of z = 0.0179 (Struble & Rood 1999). While its mass is in between the lower mass Virgo and the higher mass Coma cluster, its core reaches a density comparable to that of the Coma cluster. There are indications that Perseus is possibly more relaxed and evolved than Coma (e.g. Forman & Jones 1982). For example Perseus only has a single cD galaxy in its centre, while the core of Coma harbours two large galaxies. On the other hand, Andreon (1994) interpreted the 'non-uniform distribution of morphological types' in Perseus as an indication that this cluster is not yet virialized and instead dynamically young. This may be supported by the observation that on large scales Perseus is not a spherically symmetric cluster like Coma, but shows a projected chain of bright galaxies extending in east-west direction that is offset from the symmetric X-ray distribution.

While a significant number of regular dwarf galaxies has already been identified in a smaller field of the cluster core by Conselice et al. (2002, 2003), we focus on galaxies in the same luminosity range with $M_V > -16$ mag (corresponding to stellar masses of $M_* \lesssim 10^8$ M$_\odot$) but of fainter surface brightness and thus lower stellar density. This is made possible by our deep wide-field imaging data obtained with the 4.2 m William Herschel Telescope (WHT) Prime Focus Imaging Platform (PFIP), reaching a 5σ V-band depth of about 27 mag arcsec^{-2}. In this paper we concentrate on LSB galaxies with $\langle\mu_V\rangle_{50} \geq 24.8$ mag arcsec^{-2}, which corresponds to the currently often adopted surface brightness limit of $\mu_{g,0} \geq 24$ mag arcsec^{-2} for the so-called 'ultra-diffuse galaxies'. While the definition of the latter refers to objects with $r_{50} > 1.5$ kpc (e.g. van Dokkum et al. 2015a), we will not apply any size criterion in this study and generally speak of 'faint LSB galaxies', or 'LSB galaxies of dwarf stellar mass'. Previous work on the low mass galaxy population in Perseus includes also the 29 dwarf galaxies studied by Penny et al. (2009) and de Rijcke et al. (2009) in Hubble Space Telescope (HST) imaging data, of which six fall within our considered surface brightness range.

This paper is organized as follows: In Section 2 we describe the observations, data reduction and our final mosaic. We outline the detection of the LSB sources in Section 3, and specify their photometry in Section 4. We present our results in Section 5, where we define our sample of LSB candidates, examine their spatial distribution in the cluster, discuss peculiar candidates, and characterize their magnitude-size-surface brightness distribution in comparison to LSB candidates in the Coma cluster. We discuss our results in Section 6, followed by our conclusions in Section 7. Throughout the paper we assume a distance of 72.3 Mpc to the Perseus cluster with a scale of 20.32 kpc arcmin^{-1} (Struble & Rood 1999, using the 'cosmology-corrected' quantities from NED

with $H_0 = 73.00 \, \mathrm{km \, sec^{-1} \, Mpc^{-1}}$, $\Omega_{\mathrm{matter}} = 0.27$, $\Omega_{\mathrm{vacuum}} = 0.73$).

2 THE DATA

We acquired deep *V*-band imaging data of the Perseus cluster core with PFIP at the WHT through the Opticon program 2012B/045 (PI T. Lisker). The PFIP is an optical wide-field imaging camera with a field of view of $16 \times 16 \, \mathrm{arcmin}^2$, corresponding to $325 \times 325 \, \mathrm{kpc}^2$ at the distance of Perseus. The observations were carried out 2012 November 12 and 13. We performed dithered observations on three pointings across the cluster core, with individual exposure times of 120 s. In total 187 science exposures contribute to the final mosaic.

We reduced the data mainly with the image reduction pipeline THELI[1] (Erben et al. 2005; Schirmer 2013), which is especially designed to process wide-field imaging data. For the data reduction each exposure was spatially split into two frames, corresponding to the two detectors of the instrument. All frames were overscan- and bias-corrected, as well as flat fielded using twilight flats. To correct for remaining large scale intensity gradients that may still be imprinted in the data after flat fielding, a master background, containing only signal from the sky, was created. For the latter the sources in all frames were masked, then the frames were normalized and stacked. Assuming the background inhomogeneities are of additive nature, the master background was subsequently subtracted from all frames. Since applying one common master background was not sufficient to remove the large scale background variations from all frames, individual background models were created in a next step.

The individual models are based on object-masked frames, where the masked areas were interpolated based on values from neighbouring unmasked pixels. The resulting images were convolved with a Gaussian kernel with a full width at half-maximum (FWHM) of 512 pixels. The individual background models were subtracted from each frame. We note that the applied filter kernel is large with respect to the extent of our targets, which have typical half-light radii on the order of $20 - 60$ pixels. Then all frames were calibrated astrometrically and distortion corrected, using the Sloan Digital Sky Survey Data Release 9 (SDSS-DR9) (Ahn et al. 2012) as a reference catalogue. Finally the frames were resampled and combined to a mosaic, where each frame was weighted according to the square of its inverse sky noise.

In a second iteration of the reduction we improved the individual background models of the frames that were contaminated through the extended halos of the two brightest cluster galaxies. This optimization was done outside THELI pipeline, mainly using IRAF.[2] Manually extending the masks would have resulted in a very high fraction of masked pixels on the single frames. To avoid this, we modelled the

light distribution of both galaxies in the first iteration mosaic, using IRAF *ellipse* and *bmodel*. We then subtracted the galaxy models from the distortion corrected frames before generating new individual background models with THELI. The new background models were then subtracted from the original science frames, and combined to the second mosaic.

Lastly we corrected our mosaic for spatial zero-point variations, again outside the THELI pipeline. After selecting suitable stars in our mosaic using SEXTRACTOR (Bertin & Arnouts 1996), we measured their magnitudes with the IRAF task *photometry* on the individual flat fielded frames, before any background model was subtracted. We calculated the zero-point of each frame as median magnitude offset with respect to the SDSS-DR9 catalogue, using the transformation equations from Jester et al. (2005). The zero-point variations are then given as the deviation of the magnitude offset of individual stars from the zero-point of the respective frame. We rejected stars that deviate by more than 0.2 mag from the zero-point of the respective frame and only considered stars with small magnitude errors in both the SDSS-DR9 catalogue and the measurements with IRAF *photometry*, requiring $\sqrt{\Delta mag_{phot}^2 + \Delta mag_{SDSS}^2} < 0.05$ mag. We then established a two-dimensional map yielding the zero-point variations across the detector by fitting a two-dimensional surface to the zero-point variations obtained for all frames. Finally we divided each frame by this map, and repeated the above described reduction steps leading to the final mosaic. The zero-point of the final mosaic is 26 mag, with a mean variation of 0.02 mag with respect to the SDSS-DR9 catalogue.

Fig. 1 (left panel) shows our final deep mosaic of the Perseus cluster core (also Figs. 3 and 4). It is not centred directly on the brightest cluster galaxy NGC 1275, but on a region including the chain of luminous galaxies that are distributed to the west of it. The mosaic covers an area of $\sim 0.27 \, \mathrm{deg}^2$ ($\hat{=} 0.41 \, \mathrm{Mpc}^2$), and extends to a cluster-centric distance of $0.57°$($\hat{=} 0.70 \, \mathrm{Mpc}^2$) from NGC 1275. This corresponds to 29 per cent of the Perseus cluster virial radius for $R_{\mathrm{vir}} = 2.44 \, \mathrm{Mpc}$ (Mathews et al. 2006), or 39 per cent when adopting $R_{\mathrm{vir}} = 1.79 \, \mathrm{Mpc}$ (Simionescu et al. 2011). The mosaic reaches an image depth of $27 \, \mathrm{mag \, arcsec^{-2}}$ in the *V*-band at a signal-to-noise ratio of S/N = 1 per pixel, with a pixel scale of 0.237 arcsec pixel^{-1}. The corresponding 1σ and 5σ depths are $28.6 \, \mathrm{mag \, arcsec^{-2}}$ and $26.8 \, \mathrm{mag \, arcsec^{-2}}$, respectively. The image depth varies across the mosaic, as can be seen in the weight image (Fig. 1, right panel). The average seeing FWHM is 0.9 arcsec.

For the subsequent detection and photometry of low surface brightness sources we created one copy of the mosaic where we removed most of the sources with bright extended halos, including the largest cluster galaxies and the haloes of foreground stars. We fitted the light profiles with IRAF *ellipse*, generated models with IRAF *bmodel* and subtracted them from the mosaic.

3 DETECTION

Motivated by the detection of faint LSB galaxy candidates in the Virgo and Coma galaxy clusters by Mihos et al. (2015) and van Dokkum et al. (2015a), we inserted LSB galaxy models in the same parameter range into our mosaic and

---

[1] THELI GUI, version 2.6.2

[2] IRAF is distributed by the National Optical Astronomy Observatory, which is operated by the Association of Universities for Research in Astronomy (AURA) under a cooperative agreement with the National Science Foundation.
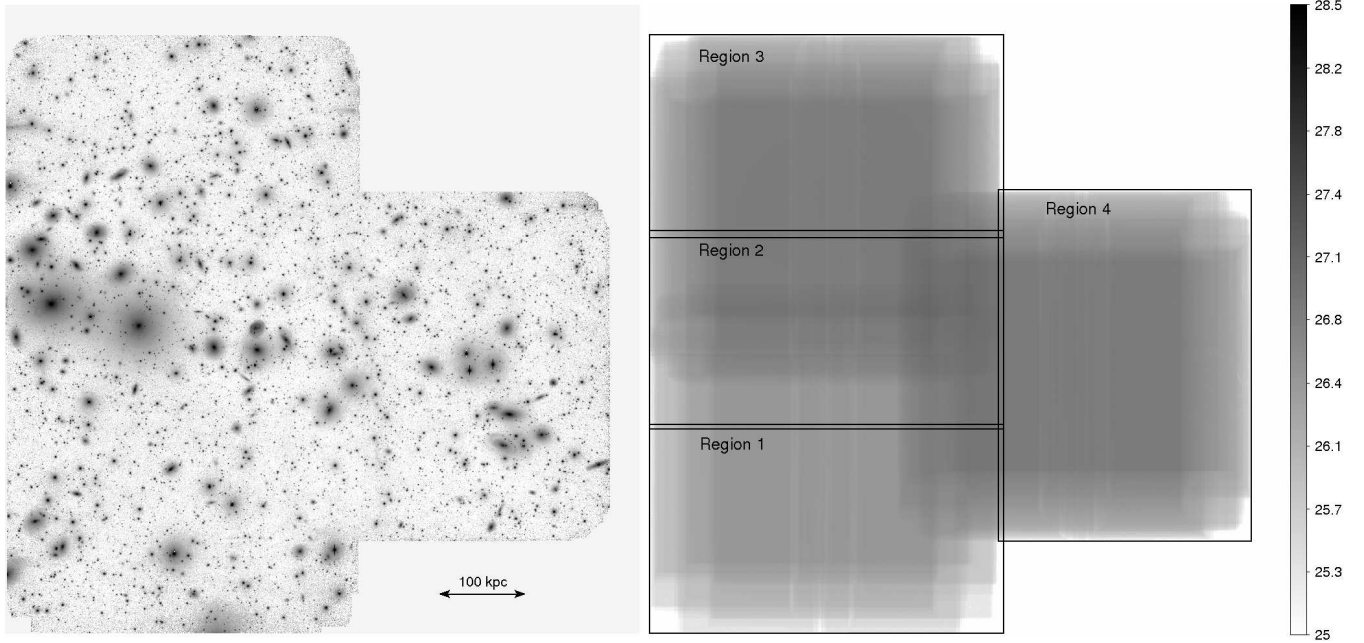
Figure 1. Deep view of the Perseus cluster core. Left: V-band mosaic. The image dimensions are $0.58° (\hat{=} 0.71\,\mathrm{Mpc}$ at $72.3\,\mathrm{Mpc})$ in east-west and north-south direction. North is up and east is to the left. The two bright galaxies in the east are NGC 1275 and NGC 1272. Right: Corresponding weight image indicating the image depth in $\mathrm{mag\,arcsec^{-2}}$ at S/N=1 per pixel (see legend on the right hand side). The black boxes indicate how we divided the mosaic into different regions for the detetcion of LSB sources (see Section 3).

then searched systematically for similarly looking objects in Perseus. We decided to search for LSB sources by eye, since automatic detection algorithms often fail in reliably detecting sources with very low S/N. We realized the models with a one component Sérsic profile of Sérsic index n=0.7-1.2 that were convolved with a Gaussian kernel, adopting our average seeing FWHM.

We generated a first set of 27 models in the parameter range $24.6 \le \langle\mu_V\rangle_{50} \le 27.8\,\mathrm{mag\,arcsec^{-2}}$, $-14 \ge M_V \ge -16.6\,\mathrm{mag}$, and $2.1 \le r_{50} \le 9.7\,\mathrm{kpc}$, assuming an average foreground extinction of $A_V = 0.5\,\mathrm{mag}$ at the location of Perseus. Among them are nine model types with different magnitudes and half-light radii. For each model type we generated two additional variants with altered position angle and ellipticity, which results in slightly different surface brightnesses. We created a second set of seven nearly round (ellipticity = 0.1) models with $\langle\mu_V\rangle_{50} \le 26.0\,\mathrm{mag\,arcsec^{-2}}$ that extend the parameter range to smaller half-light radii of 1.5 kpc and fainter magnitudes of $-13.5\,\mathrm{mag}$.

From the first model set we always inserted 30-40 models of one type, i.e. with the same magnitude and half-light radius but varying ellipticity, into one copy of the mosaic. We generated two additional mosaic copies where we inserted the models from the second model set. We used these copies only at a later stage to focus the detection especially on smaller and fainter LSB sources that turned out to be quite numerous based on the search using the first model set. In total we inserted 305 models from the first model set into nine different mosaic copies, and 56 models from the second set into two further copies.

To facilitate the visual detection of LSB sources, we used the mosaic variant where we previously fitted and subtracted the light distribution of most of the extended sources

(see Section 2). To remove the remaining bright sources on each copy of the mosaic, we ran SExtractor to detect all sources with more than ten pixels above a detection threshold of $1.5\,\sigma$, and replaced the pixels above this threshold with zero values, corresponding to the background level of our mosaic. We then convolved the data with a circular Gaussian kernel with $\sigma = 1$ pixel, and demagnified each copy by a factor of 1.5. We further divided each mosaic copy into four smaller regions of different image depth according to the weight image (see Fig.1, right panel). Finally two of us independently searched visually for diffuse sources in each copy, thereby detecting simultaneously the inserted models and real LSB candidates, without knowing where the former had been inserted. After removing sources that we identified more than once in different copies of the same region, this resulted in a preliminary sample of 214 LSB sources that were identified by at least one of us, and for which we carried out photometry (see Section 4).

We used the visually identified models from the first model set to get a rough estimate on our detection rate (see Fig. 2). We estimated the detection rate for each model type as fraction of the total number of inserted models that were visually identified. We find that the detection rate generally drops with surface brightness. We detected more than 90 per cent of all models with $\langle\mu_V\rangle_{50} < 25.5\,\mathrm{mag\,arcsec^{-2}}$, between 70 and 90 per cent of all models with $25.5 \le \langle\mu_V\rangle_{50} < 27.0\,\mathrm{mag\,arcsec^{-2}}$, and about 50 per cent of all models with $\langle\mu_V\rangle_{50} > 27.0\,\mathrm{mag\,arcsec^{-2}}$.[3]

The models with $\langle\mu_V\rangle_{50} < 27.0\,\mathrm{mag\,arcsec^{-2}}$ are in gen-

---

[3] The given surface brightnesses refer to the average surface brightness of the three model variants with different ellipticity, and thus surface brightness, that exist per model type.
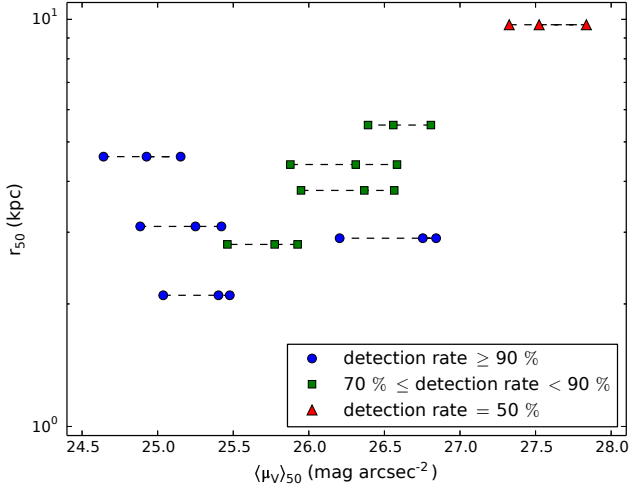
Figure 2. Detection rates of visually identified model galaxies as a function of half-light radius and surface brightness. The detection rates are based on 30-40 models of one type, with the same half-light radius and magnitude, but varying ellipticity and thus surface brightness, that were inserted into one copy of the mosaic, respectively. Models of the same type are connected through dashed lines in the plot. The total number of inserted models is 305.

eral clearly visible in our data and the main reason for missing some of them seems to be related to overlap with brighter sources. We estimated the area occupied by remaining bright extended sources in our object-subtracted mosaic to be 12 per cent[4], which compares to an average detection rate of 90 per cent of all models with $\langle\mu_V\rangle_{50} < 27.0\,\mathrm{mag\,arcsec^{-2}}$. Scatter in the trend of decreasing detection fraction with surface brightness can both be caused by our approach of visual source detection, as well as by the different overlap fractions of the inserted models with brighter sources.[5] The detection rate of models with $\langle\mu_V\rangle_{50} < 27.0\,\mathrm{mag\,arcsec^{-2}}$ is similar in all regions of our mosaic, even in the shallowest region (*Region 1*; see Fig.1, right panel). For models with $\langle\mu_V\rangle_{50} > 27.0\,\mathrm{mag\,arcsec^{-2}}$ we find, however, a lower detection rate in *Region 1* and *Region 2*, compared to the other two regions. While *Region 1* is the shallowest region, the lower detection rate in *Region 2* might be related to the higher galaxy density compared to the other regions.

4 PHOTOMETRY

Photometry of LSB sources is challenging and the measurements suffer in general from higher uncertainties compared to sources of higher surface brightness. One reason for this is that the radial flux profile of the former is characterized by a larger fraction of flux at large radii, where the S/N is typically very low. This also implies that contamination

---

[4] This accounts for all sources that were detected with SExtractor with more than 1000 connected pixels above a detection threshold of $1.5\,\sigma$.

[5] We note that the fraction of models whose center overlaps with one of the SExtractor-detected sources above $1.5\,\sigma$ does not exceed 12 per cent per model type.

from close neighbour sources and the presence of background gradients is more severe for these objects. We quantify the arising uncertainties in our data using inserted LSB galaxy models (see Section 5.3).

We derived magnitudes and sizes from growth curves through iterative ellipse fitting with IRAF *ellipse*, rather than from fits to analytical models. The first step was to obtain a first guess of the centre, ellipticity and position angle of all sources. We used SExtractor to measure the parameters of 131 objects that were detected with a detection threshold of $1\,\sigma$ (128 objects) or $0.8\,\sigma$ (3 objects). For 83 objects that were not detected with SExtractor or that had obviously wrong parameters we estimated their centre and shape visually based on the Gaussian smoothed and demagnified mosaic. Then we ran *ellipse* with fixed parameters, adopting the previously measured or estimated centres, ellipticities and position angles. We chose a linear step-size of 5 pixels for consecutive isophotes. We used the first ellipse fit results to generate 2-dimensional brightness models with IRAF *bmodel* that we subtracted from the fitted source.

The residual images served as a basis to create masks of neighbouring sources from SExtractor segmentation images. We ran SExtractor in two passes, one with a minimum number of 28 connected pixels above a detection threshold of $1\,\sigma$, the other with a lower detection threshold of $0.6\,\sigma$ and requiring a minimum number of 1000 connected pixels. In both passes we used SExtractor with the built-in filtering prior to detection. We combined both segmentation images and extended the masked areas by smoothing with a Gaussian kernel. We ran *ellipse* in a second pass with the masks to exclude that flux from neighbouring sources contributes to the ellipse fits. From the second iteration residual images we created improved masks where the masked regions are somewhat larger. We unmasked the centre of nucleated candidates and ellipse fit residuals when necessary.

The next step was to determine the background level from the third pass ellipse fit results using the improved masks. Getting the background level right is a very subtle task and the major source of the uncertainties in the magnitude and size measurements. Therefore we determined the background level for each of our detected LSB objects individually. We first measured the radial flux profiles out to large radii (350 pixels) for each object. We then manually adjusted the radius and width of the background annulus, whose median flux we adopted as the background level. The inner radius of the background annulus was set at the first break in the flux profile where the intensity gradient significantly changes and the flux profile levels out. We set the width of the annulus to 50 pixels. Its shape follows the ellipticity and position angle of the measured object.

Although all neighbour sources were carefully masked, still some flux profiles show signs of contamination. Especially at larger radii where faint flux levels are reached, the flux of the LSB source can be comparable to the flux of a neighbour source that still extends beyond the masked area (e.g. some very extended haloes of foreground stars or bright cluster galaxies). Also background inhomogeneities remaining in the data after the reduction can contaminate the flux profiles. Possible contamination can become apparent in a flux profile when, for example, the profile continues to decline after the first break instead of levelling out to zero. In

this case we nevertheless set the inner radius of the background annulus to the first break in the profile, and eventually decrease its width to make sure that the flux profile is flat in this region.

Even though we might truncate a galaxy at too high intensity, resulting in a systematically fainter magnitude and a smaller half-light radius, restricting the analysis to the uncontaminated inner profile helps to preserve the true surface brightnesses (see the right panels in Fig. 6 and Section 5.3). After subtracting the background offset, we then obtained a first estimate of the magnitudes and sizes by running *ellipse* in a fourth pass on the background corrected images and taking into account the masked sources. We determined the total flux from the cumulative flux profile[6] and derived the half-light radius along the semi-major axis, as well as the mean effective surface brightness within one half-light radius.

In the final iteration we measured the centre, ellipticity and position angle of our LSB sources more accurately, using our first guess parameters as input values. We used `IRAF` *imcentroid* to derive the centre, and calculated the ellipticity and position angle from the image moments within a circular area defined by our first-guess half-light radius. We also further improved the masks by manually enlarging the masks of extended neighbour sources with faint haloes.[7] After that we ran *ellipse* in a fifth pass with the new parameters and masks to adjust the inner radius of the background annulus. We adopted the new background level and derived the final magnitudes, half-light radii and mean effective surface-brightnesses in a last pass of ellipse fitting. We corrected the derived magnitudes for extinction, using the IRSA Galactic Reddening and Extinction Calculator, with reddening maps from Schlafly & Finkbeiner (2011). The average foreground extinction of our measured sources is $A_V = 0.5$ mag.

5 FAINT LSB GALAXIES IN THE PERSEUS CLUSTER CORE

5.1 Sample

We define our sample of low surface brightness galaxy candidates to include all objects with $\langle\mu_V\rangle_{50} \geq 24.8$ mag arcsec^{-2}. This corresponds to the currently often adopted surface brightness limit of $\mu_{g,0} \geq 24.0$ mag arcsec^{-2} for 'ultra-diffuse galaxies' (e.g. van Dokkum et al. 2015a), when assuming an exponential profile with Sérsic $n = 1$ (cf. Graham & Driver 2005), $g - r = 0.6$ and using the transformation equations from Jester et al. (2005). Of our preliminary sample, 133 objects fall into this parameter range. We carefully examined all of them, both on the original as well as on the smoothed and demagnified mosaic. We also compared them to an independent dataset of the Perseus cluster, obtained with

WIYN/ODI in the g,r and i filters (program 15B-0808/5, PI: J. S. Gallagher). Since the single-band images are shallower than our data, we used the stacked g,r,i images for the comparison.

Based on a more detailed visual examination of their morphology, we classified 82 of our candidates as likely galaxies. They are characterized by a smooth morphology and are confirmed in the independent dataset. We classified seven further candidates as possible galaxies (all of them are shown in Fig. 3 in the bottom row). Three of them (candidates 26, 31 and 44) are clearly visible in our data, but their morphology does not appear very regular. Since these objects are also visible in the WIYN/ODI data, we rule out that they are image artefacts. However a confusion with cirrus cannot be excluded (see Section 5.3). The four other candidates (candidates 27, 49, 57 and 81) are classified as possible galaxies since they are only barely visible in our data, due to their low surface brightness or low S/N, and are not confirmed in the shallower independent dataset. We rejected 44 LSB sources from our sample, since we cannot exclude that these are remaining background inhomogeneities from the reduction, or residuals from ellipse fitting of the brighter galaxies. Most of them are of very diffuse nature (80 per cent have $\langle\mu_V\rangle_{50} \geq 26.5$ mag arcsec^{-2}) and often do not have a smooth morphology.

Our final sample includes 89 LSB galaxy candidates in the Perseus cluster core. We show our sample in Fig. 3 and provide the photometric parameters in Table 1. We also compare our sample to overlapping HST/ACS images, in order to investigate whether some of our objects would classify as background sources, based on possible substructure in the form of, e.g., spiral arms. Seven of our LSB candidates fall on HST/ACS pointings, and none of them shows signs of substructure. We therefore expect that the overall contamination through background galaxies is low in our sample, based on the morphological appearance in the HST as well as in the WHT images and due to the location of our sample in the core region rather than in the cluster outskirts. Certain cluster membership can, however, only be established through measurements of radial velocities. The six brightest candidates in the HST/ACS images with $24.8 \leq \langle\mu_V\rangle_{50} \leq 25.4$ mag arcsec^{-2}, as measured in our data, were previously identified in Penny et al. (2009) (candidates 62, 64, 69, 70, 73 and 87). One of them (candidate 62) was first catalogued by Conselice et al. (2002, 2003). The faintest candidate, with $\langle\mu_V\rangle_{50} = 26.5$ mag arcsec^{-2} (candidate 82), is only barely visible in the HST/ACS images and was not published previously.

5.2 Properties

Fig. 4 shows the spatial distribution of our sample of 89 faint LSB galaxy candidates in the Perseus cluster core. The sample spans a range of $47 \leq d \leq 678$ kpc in projected cluster-centric distance, with respect to the cluster's X-ray centre[8] (Piffaretti et al. 2011). This corresponds to $0.02 - 0.28\,R_{vir}$ when assuming a virial radius of $R_{vir} =$

---

[6] We adopted the median of the cumulative fluxes `TFLUX_E` from the ellipse fit tables, namely of the five isophotes between the inner radius of the background annulus and 20 pixels further, as an estimate of the total flux. Since *ellipse* does not account for masked regions when calculating the total flux within an isophote, we replaced the masked regions with values from the 2-D model created with `IRAF` *bmodel* from the radial flux profile.

[7] Using ds9 regions (Joye & Mandel 2003) and `IRAF` *mskregions*.

[8] The X-ray centroid almost coincides with the optical location of NGC 1275.

Table 1. Coordinates and structure parameters of faint LSB galaxy candidates in the Perseus cluster core. M_V and $\langle\mu_V\rangle_{50}$ are corrected for Galactic foreground extinction. A_V is derived from the reddening maps of Schlafly & Finkbeiner (2011). No reliable individual errors can be provided, but the right panels in Fig. 6 illustrate the statistical and systematic uncertainties for LSB galaxy models in the parameter range of our sample; details are provided in Section 5.3. The table is sorted by increasing right ascension.

ID	R.A. (J2000)	Dec. (J2000)	$\langle\mu_V\rangle_{50}$ (mag arcsec^{-2})	M_V (mag)	A_V (mag)	r_{50} (kpc)	Ellipticity
1	03 17 00.37	+41 19 20.6	24.9	-15.0	0.4	1.9	0.08
2	03 17 03.26	+41 20 29.1	25.9	-12.9	0.4	1.2	0.20
3	03 17 04.42	+41 30 39.2	25.2	-12.7	0.4	0.8	0.17
4	03 17 07.13	+41 22 52.5	25.2	-14.5	0.4	1.7	0.08
5	03 17 11.02	+41 34 03.3	25.3	-14.3	0.4	1.7	0.13
6	03 17 13.29	+41 22 07.6	25.3	-12.9	0.4	0.9	0.10
7	03 17 15.97	+41 20 11.7	25.1	-15.1	0.4	2.1	0.05
8	03 17 19.71	+41 34 32.5	26.3	-13.7	0.4	2.1	0.21
9	03 17 23.50	+41 31 40.1	25.1	-14.2	0.4	1.4	0.01
10	03 17 24.94	+41 26 09.7	25.1	-13.6	0.4	1.1	0.17
11	03 17 35.49	+41 18 12.7	25.2	-13.6	0.4	1.1	0.05
12	03 17 36.78	+41 23 01.6	25.2	-14.0	0.4	1.4	0.09
13	03 17 38.21	+41 31 56.9	25.1	-13.6	0.4	1.1	0.13
14	03 17 39.22	+41 31 03.5	25.9	-13.9	0.4	1.7	0.09
15	03 17 39.42	+41 24 45.0	25.5	-13.7	0.4	1.3	0.13
16	03 17 41.79	+41 24 01.9	25.8	-13.2	0.4	1.2	0.12
17	03 17 44.16	+41 21 18.4	25.0	-14.4	0.4	1.5	0.15
18	03 17 48.34	+41 18 38.9	25.9	-14.1	0.4	2.0	0.13
19	03 17 53.17	+41 19 31.9	25.5	-13.9	0.4	1.4	0.03
20	03 17 54.66	+41 24 58.8	25.2	-13.3	0.4	1.0	0.07
21	03 18 00.81	+41 22 23.0	24.9	-13.6	0.4	1.0	0.11
22	03 18 05.55	+41 27 42.4	25.8	-14.2	0.5	2.1	0.25
23	03 18 09.55	+41 20 33.5	26.4	-12.2	0.5	1.0	0.12
24	03 18 13.08	+41 32 08.3	25.3	-13.8	0.5	1.3	0.11
25	03 18 15.44	+41 28 35.2	24.9	-13.4	0.5	0.9	0.17
26	03 18 19.50	+41 19 24.8	26.5	-13.8	0.5	2.3	0.15
27	03 18 20.79	+41 45 29.3	26.3	-14.0	0.4	2.3	0.14
28	03 18 21.66	+41 45 27.6	25.9	-13.9	0.4	1.8	0.13
29	03 18 23.33	+41 45 00.6	25.6	-14.7	0.4	2.2	0.04
30	03 18 23.40	+41 36 07.7	25.6	-12.3	0.5	0.7	0.08
31	03 18 24.32	+41 17 30.7	26.0	-15.5	0.5	4.1	0.17
32	03 18 24.46	+41 18 28.4	26.5	-13.0	0.5	1.5	0.09
33	03 18 25.86	+41 41 06.9	25.5	-14.0	0.5	1.5	0.06
34	03 18 26.92	+41 14 09.5	25.7	-12.4	0.5	0.8	0.03
35	03 18 28.18	+41 39 48.5	25.8	-13.9	0.5	1.9	0.21
36	03 18 29.19	+41 41 38.9	26.2	-13.1	0.5	1.4	0.04
37	03 18 30.36	+41 22 29.8	25.9	-12.1	0.5	0.8	0.13
38	03 18 32.11	+41 27 51.5	25.4	-13.1	0.5	0.9	0.05
39	03 18 32.13	+41 32 12.3	25.2	-12.8	0.5	0.8	0.19
40	03 18 33.25	+41 40 56.1	25.2	-13.9	0.5	1.3	0.12
41	03 18 33.57	+41 41 58.3	25.2	-13.4	0.5	1.0	0.06
42	03 18 33.60	+41 27 45.5	25.1	-13.5	0.5	1.0	0.04
43	03 18 34.57	+41 24 18.6	26.1	-12.9	0.5	1.3	0.19
44	03 18 34.73	+41 22 40.5	27.1	-13.6	0.5	2.6	0.09
45	03 18 36.14	+41 21 59.4	26.2	-13.9	0.5	2.2	0.22
46	03 18 37.51	+41 24 16.0	26.3	-11.8	0.5	0.8	0.03
47	03 18 38.96	+41 30 06.8	26.6	-12.8	0.5	1.5	0.13
48	03 18 39.53	+41 39 30.4	25.8	-12.6	0.5	1.0	0.20
49	03 18 39.84	+41 38 58.4	27.1	-12.7	0.5	1.9	0.26
50	03 18 39.92	+41 20 09.0	26.3	-13.2	0.5	1.5	0.11
51	03 18 41.38	+41 34 01.3	25.5	-13.7	0.5	1.5	0.27
52	03 18 42.60	+41 38 33.0	26.1	-12.3	0.5	0.9	0.04
53	03 18 44.65	+41 34 07.7	25.4	-13.5	0.5	1.2	0.09
54	03 18 44.95	+41 24 20.4	24.9	-13.9	0.5	1.1	0.11
55	03 18 46.16	+41 24 37.1	26.2	-14.3	0.5	2.4	0.09
56	03 18 48.02	+41 14 02.4	25.9	-14.3	0.5	2.3	0.23
57	03 18 48.43	+41 40 35.1	27.1	-13.3	0.5	2.4	0.11
58	03 18 50.74	+41 23 09.1	25.4	-13.0	0.4	1.0	0.17
59	03 18 54.32	+41 15 29.2	24.9	-14.0	0.5	1.1	0.02

Table 1 – *continued*

ID	R.A. (J2000)	Dec. (J2000)	$\langle\mu_V\rangle_{50}$ (mag arcsec^{-2})	M_V (mag)	A_V (mag)	r_{50} (kpc)	Ellipticity
60	03 18 55.38	+41 17 50.0	25.8	-12.5	0.5	1.0	0.18
61	03 18 59.40	+41 25 15.4	26.0	-12.5	0.4	1.0	0.07
62	03 18 59.42	+41 31 18.7	25.4	-13.9	0.4	1.4	0.07
63	03 19 01.50	+41 38 59.0	25.8	-12.9	0.5	1.1	0.17
64	03 19 05.83	+41 32 34.4	24.8	-13.8	0.4	1.1	0.09
65	03 19 07.77	+41 27 12.1	24.8	-12.9	0.4	0.7	0.06
66	03 19 09.32	+41 41 51.7	25.9	-12.5	0.5	0.9	0.06
67	03 19 12.76	+41 43 30.0	25.2	-13.5	0.5	1.1	0.08
68	03 19 15.01	+41 22 31.7	25.1	-13.3	0.4	0.9	0.06
69	03 19 15.70	+41 30 34.6	25.1	-12.9	0.4	0.8	0.05
70	03 19 15.86	+41 31 05.8	25.2	-14.2	0.4	1.4	0.03
71	03 19 16.02	+41 45 45.9	26.1	-13.3	0.5	1.4	0.05
72	03 19 17.53	+41 12 41.3	26.7	-12.8	0.4	1.5	0.02
73	03 19 17.83	+41 33 48.4	24.9	-13.7	0.4	1.0	0.07
74	03 19 21.94	+41 27 22.5	24.9	-14.7	0.4	1.7	0.15
75	03 19 23.06	+41 23 16.8	26.3	-13.7	0.4	2.1	0.20
76	03 19 23.12	+41 38 58.7	26.0	-13.4	0.5	1.5	0.11
77	03 19 32.76	+41 36 12.8	25.7	-13.6	0.4	1.4	0.09
78	03 19 33.80	+41 36 32.5	24.8	-13.6	0.5	1.1	0.34
79	03 19 39.19	+41 12 05.6	25.4	-14.4	0.4	1.8	0.06
80	03 19 39.22	+41 13 43.5	26.3	-12.8	0.4	1.3	0.07
81	03 19 44.03	+41 39 18.4	26.9	-13.8	0.4	2.7	0.14
82	03 19 45.66	+41 28 07.3	26.1	-13.9	0.4	2.0	0.13
83	03 19 47.45	+41 44 09.3	26.0	-12.9	0.4	1.2	0.07
84	03 19 49.70	+41 43 42.6	24.8	-13.5	0.4	0.9	0.05
85	03 19 50.13	+41 24 56.3	25.5	-13.7	0.4	1.3	0.05
86	03 19 50.56	+41 15 33.4	25.6	-12.1	0.4	0.7	0.17
87	03 19 57.41	+41 29 31.2	25.0	-13.3	0.4	0.9	0.05
88	03 19 59.10	+41 18 33.1	24.8	-15.5	0.4	2.2	0.02
89	03 20 00.20	+41 17 05.1	25.7	-13.5	0.4	1.4	0.10

2.44 Mpc (Mathews et al. 2006). About half of our sample is located closer than 330 kpc to the cluster centre.

We find three LSB candidates that appear to be associated with structures resembling tidal streams (see Fig. 4, right panels). Candidate 44 seems to be embedded in diffuse filaments, candidates 26 and 31 appear connected via an arc-shaped stream. We find one further galaxy with tidal tails (see Fig. 4, bottom left panel), which has a slightly brighter surface brightness of $\langle\mu_V\rangle_{50} = 24.4$ mag arcsec^{-2} and therefore was not included in our sample. We will analyse faint cluster galaxies with brighter surface brightnesses in a future paper. It is noticeable that all four objects are confined within one region to the south-west of the cluster centre, within a cluster-centric distance range of about $300-400$ kpc. Also the peculiar more luminous galaxy SA 0426-002 (cf. Conselice et al. 2002; Penny et al. 2014) falls on our mosaic, which shows a disturbed morphology with extended low surface brightness lobes (see Fig. 4, top left panel).

We show the radial projected number density distribution of our sample in Fig. 5. It was derived by dividing the number of galaxies in radial bins of a width of 100 kpc by the area of the respective bin that falls on our mosaic. The bins are centred on the Perseus X-ray centre. We find that the number density is nearly constant for cluster-centric distances $r \geq 100$ kpc, but drops in the very centre at

$r < 100$ kpc,[9] with a statistical significance of $2.8\,\sigma$ with respect to the average number density at larger radii. For comparison, a preliminary analysis showed that the distribution of bright cluster members is consistent with the expectation of being much more centrally concentrated.

Fig. 6 shows the magnitude-size and magnitude-surface brightness distribution of our Perseus cluster LSB galaxy sample. We include the Coma cluster LSB galaxies and candidates from van Dokkum et al. (2015a) and the three very low surface brightness galaxy candidates in Virgo from Mihos et al. (2015). For comparison we also show Virgo cluster early and late type galaxies (compilation of Lisker et al. 2013; based on the Virgo Cluster Catalogue (VCC), Binggeli et al. 1985), Virgo cluster dSphs (Lieder et al. 2012), as well as dSphs from the Local Group (McConnachie 2012).

Our sample spans a parameter range of $24.8 \leq \langle\mu_V\rangle_{50} \leq 27.1$ mag arcsec^{-2}, $-11.8 \geq M_V \geq -15.5$ mag and $0.7 \leq r_{50} \leq 4.1$ kpc. The surface brightness range of our sample is comparable to the LSB galaxy sample from van Dokkum et al. (2015a) and approaches the surface brightness of the two brighter Virgo LSB candidates from Mihos et al. (2015). With regard to magnitudes and sizes our sample includes smaller and fainter LSB candidates than the sample from

---

[9] Only two galaxies are contained in the central bin with $r < 100$ kpc.
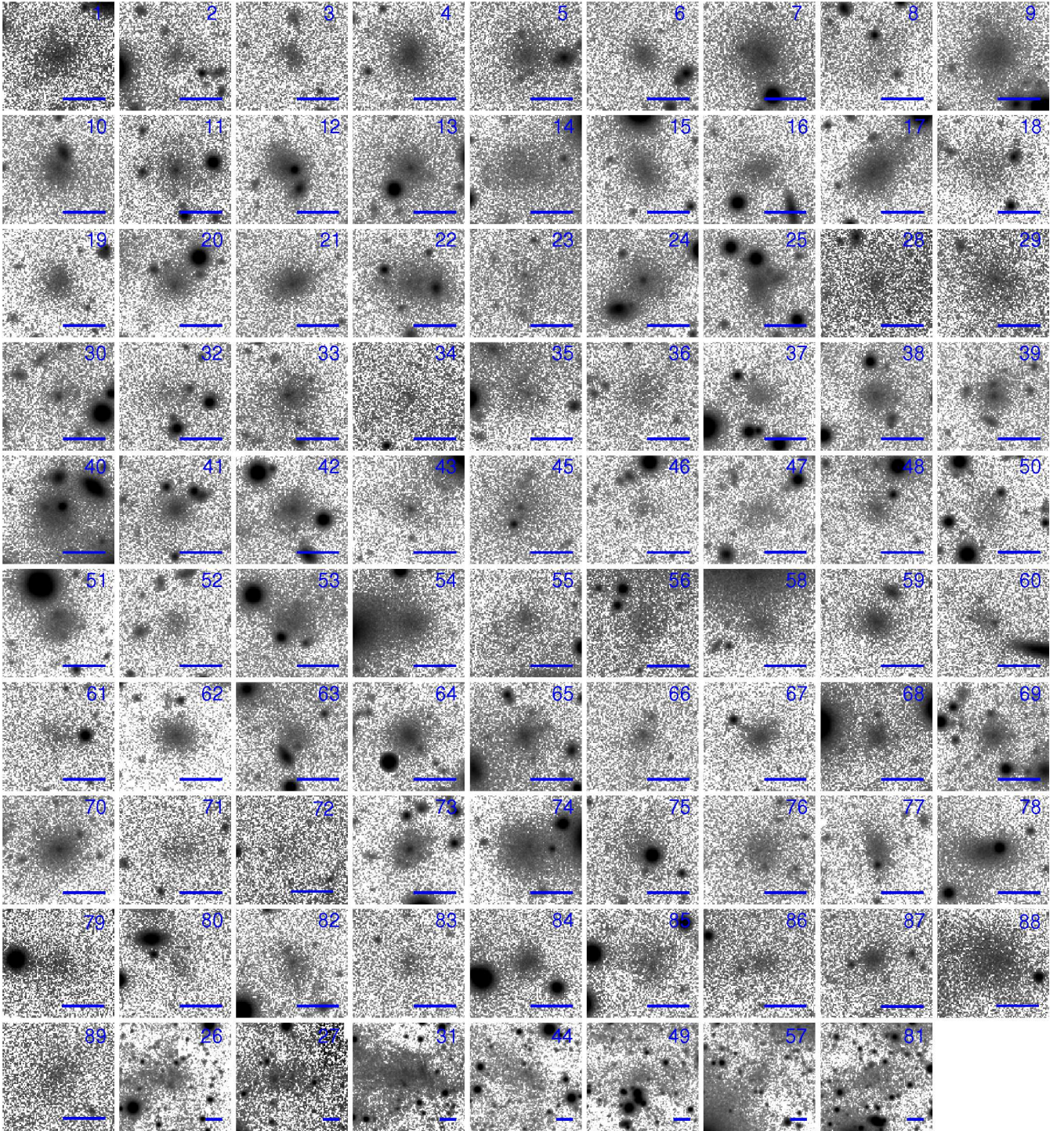
Figure 3. Sample of faint LSB galaxy candidates in the Perseus cluster core. The first 82 panels show LSB candidates in cutout regions of our original data with a size of $21 \times 21 \, \mathrm{arcsec}^2$, respectively. The seven last panels in the bottom row show LSB candidates classified as possible galaxies (see Section 5.1). They are displayed in our smoothed and demagnified data in cutout regions with a size of $53 \times 53 \, \mathrm{arcsec}^2$, respectively. The blue bar in each panel of the figure denotes a length of $3 \, \mathrm{kpc}$. The number in each panel corresponds to the ID of the shown object given in Table 1. North is up and east is to the left.

van Dokkum et al. (2015a), which is likely due to their resolution limit. At faint magnitudes our samples overlaps with the parameter range of cluster and Local Group dSphs. We note that the apparent relation between magnitude and size of our sample is created artificially. The bright surface

brightness limit arises due to our definition of including only sources fainter than $\langle \mu_V \rangle_{50} = 24.8 \, \mathrm{mag \, arcsec}^{-2}$ in our sample. The faint limit is due to our detection limit.

At brighter magnitudes $M_V \leq -14 \, \mathrm{mag}$, the LSB candidates of our sample are systematically smaller at a given
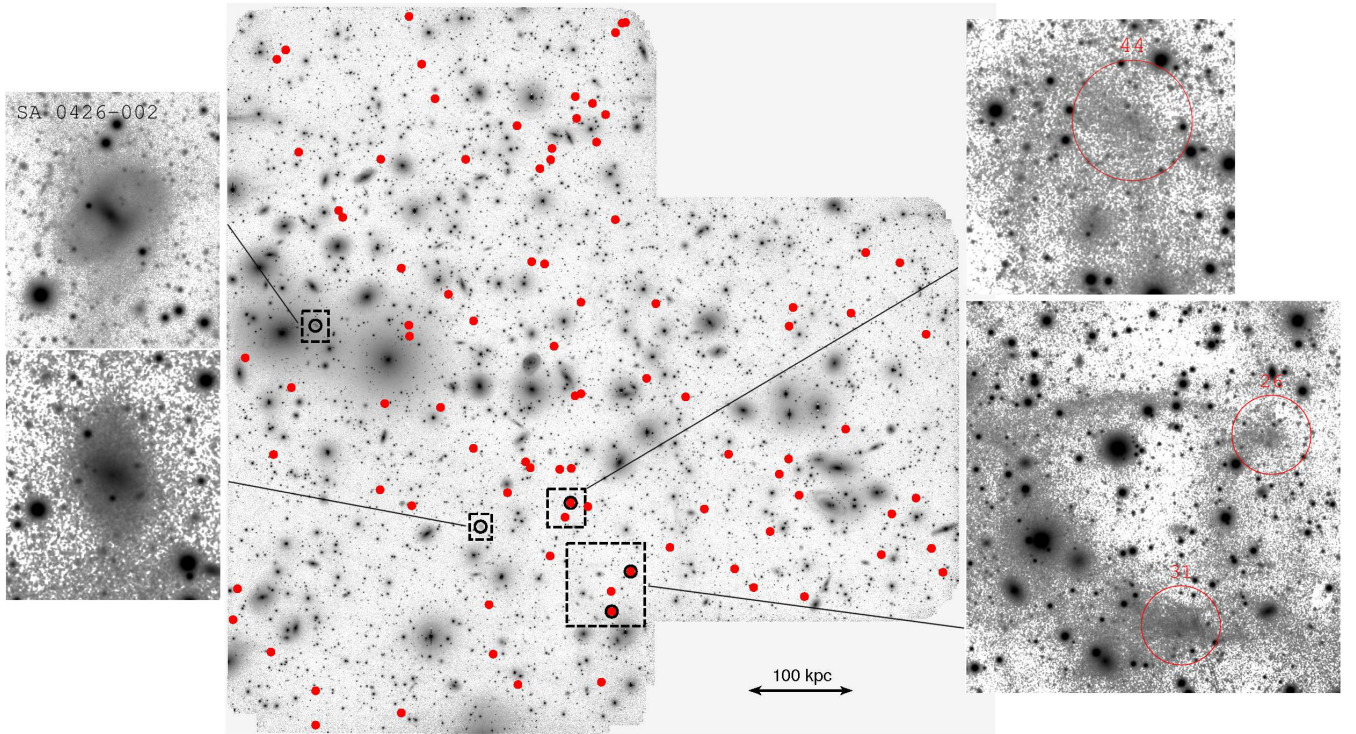
Figure 4. Spatial distribution of LSB galaxy candidates in the Perseus cluster core (central panel) and candidates with signs of possible tidal disruption (side panels). Red dots indicate our sample of LSB candidates. The dashed squares on the mosaic indicate the size of the cutout regions shown on the side panels. The images on the side panels were smoothed except the image in the top left side panel, which shows a cutout from the original data. The red dots with black circles mark the positions of candidates 26, 31 and 44 shown in the side panels on the right hand side. The two galaxies with the tidal structures in the left side panels are not part of our LSB galaxy sample. The image height and width of the mosaic is $0.58\,\mathrm{deg}$ ($\hat{=}\,0.71\,\mathrm{Mpc}$). North is up and east is to the left.
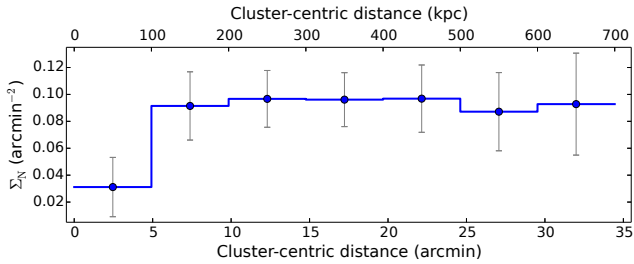
Figure 5. Radial projected number density distribution as a function of cluster-centric distance of our sample of LSB galaxy candidates in the Perseus cluster core. The radial bins have a width of 100 kpc. Shown are the statistical error bars.

magnitude than the LSB candidates identified in the Coma cluster, with all but one LSB candidate having $r_{50} < 3\,\mathrm{kpc}$. However, van Dokkum et al. (2015a) cover a much larger area of the Coma cluster, while we only surveyed the core region of Perseus.[10] Our total observed area corresponds to $0.41\,\mathrm{Mpc}^2$. This translates to a circular equivalent area with a radius of $R = 0.15\,\mathrm{R_{vir,Perseus}}$, when assuming a virial ra-

dius for Perseus of $\mathrm{R_{vir,Perseus}} = 2.44\,\mathrm{Mpc}$ (Mathews et al. 2006).[11]

When selecting all LSB candidates from the van Dokkum et al. (2015a) sample that are located in the core of Coma, within a circular area with cluster-centric distances smaller than $R = 0.15\,\mathrm{R_{vir,Coma}}$, where $\mathrm{R_{vir,Coma}} = 2.8\,\mathrm{Mpc}$ (Łokas & Mamon 2003), seven LSB candidates remain. These are marked with black squares in Fig. 6. One can see that also only two of them reach sizes of $r_{50} > 3\,\mathrm{kpc}$. Since the sample of van Dokkum et al. (2015a) has a brighter magnitude and larger size limit than our study, we restrict the comparison to objects with $M_V \leq -14\,\mathrm{mag}$ and $r_{50} \geq 2\,\mathrm{kpc}$, which should well have been detected by van Dokkum et al. (2015a). Five LSB candidates in the Coma cluster core are in this parameter range, whereas in Perseus we find seven. A similar result is obtained when comparing to the independent sample of Coma cluster LSB galaxy candidates from Yagi et al. (2016). When selecting LSB candidates of the Coma core region in the same surface brightness range as our sample and with $M_V \leq -14\,\mathrm{mag}$ and $r_{50} \geq 2\,\mathrm{kpc}$, we find ten LSB candidates in this parameter range, where three LSB candidates have $r_{50} \geq 3\,\mathrm{kpc}$. While it seems that the Virgo cluster galaxies shown in Fig. 6 are also rare in this

[10] According to tests with the inserted model galaxies (see Section 3) sources in the surface brightness range of the LSB galaxy sample from van Dokkum et al. (2015a) can easily be detected in our data.

[11] We note that our field is not centred directly on the cluster centre, but extends to the west of it.
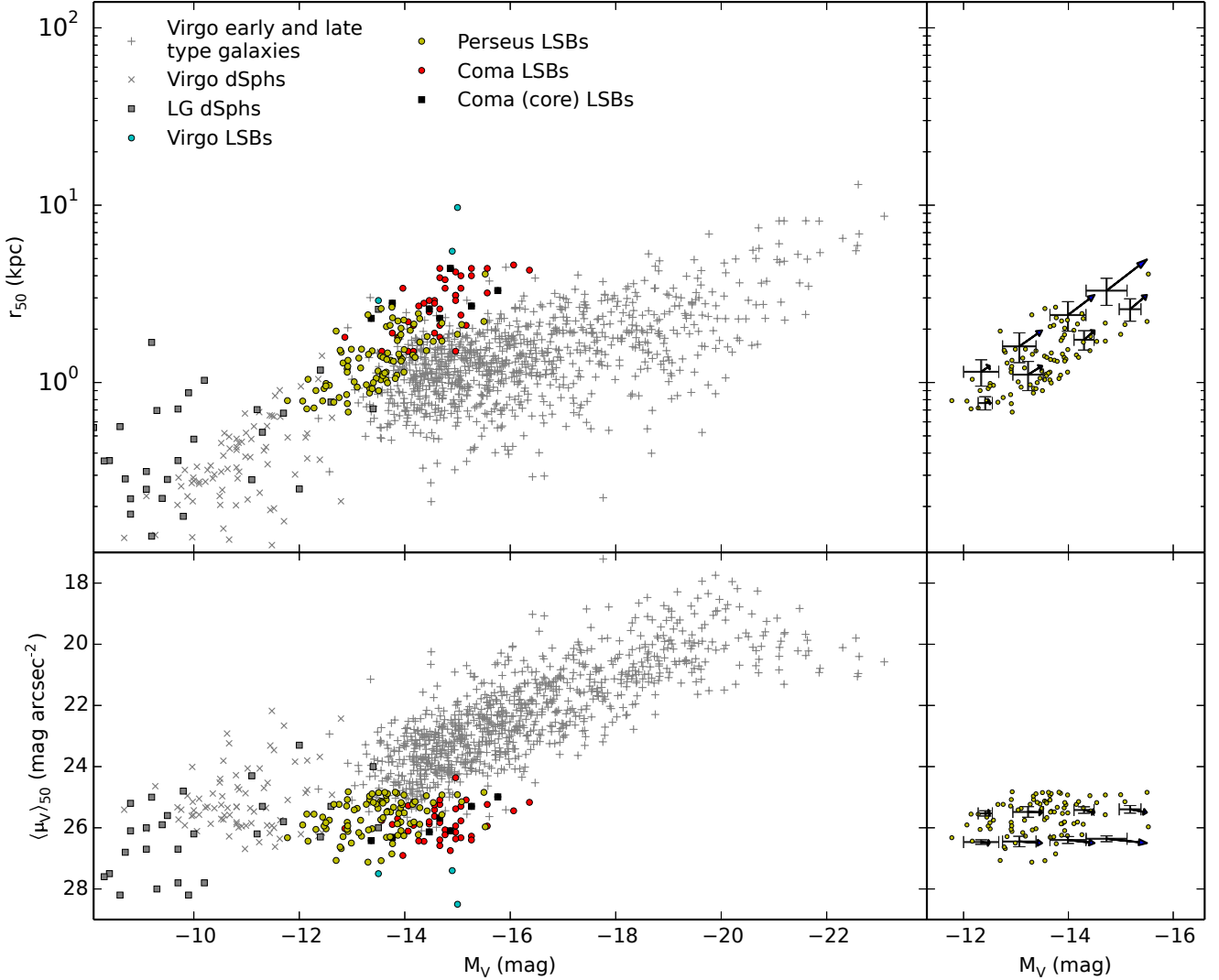
Figure 6. Structural parameters of faint LSB galaxy candidates in the Perseus cluster core (left panels). We compare our sample to LSB galaxy candidates in the Virgo cluster (Mihos et al. 2015), and to LSB galaxies and candidates in the Coma cluster (van Dokkum et al. 2015a). We mark those LSB objects in Coma that are located in the cluster core within a circular area with a radius of $R = 0.15\ R_{vir,Coma}$. This corresponds to an area of similar extent as our observed area of the Perseus cluster core (see Section 5.2). For comparison we also show early and late type galaxies from the Virgo cluster (compilation of Lisker et al. 2013; based on the VCC), Virgo dSphs (Lieder et al. 2012) and dSphs from the Local Group (McConnachie 2012). We transformed the magnitudes of the LSB candidates from van Dokkum et al. (2015a) and the galaxies from Lisker et al. (2013) with the transformation equations from Jester et al. (2005). For the former we assumed $g - r = 0.6$, for the latter we used the measured $g - r$ colors. The two panels on the right hand side show our typical uncertainties that occur for LSB galaxy models ($n = 1$, ellipticity $= 0.1$) in the parameter range of our sample (see Section 5.3). We created eight model types with different parameters. Each model type was inserted ten times at different positions into one copy of our mosaic. The black arrows indicate our systematic parameter uncertainties. The arrow tips point to the true parameters of the models, the endpoints represent the average measured parameter values of the ten inserted models of each type. On average the measured M_V values are by 0.4 mag too faint, the measured r_{50} values are underestimated by 0.5 kpc, and the measured $\langle\mu_V\rangle_{50}$ values are by 0.1 mag arcsec^{-2} too bright. The error bars represent our statistical uncertainties, and were calculated as standard deviation of the measured values of each model type.

parameter range, we note that the catalogue we used is not complete at magnitudes fainter than $M_r = -15.2$ mag.

Thus, in summary we find that firstly, the core regions of the Perseus and the Coma cluster harbour a similar number of faint LSB galaxy candidates in the same parameter range of $M_V \leq -14$ mag and $r_{50} \geq 2$ kpc, and secondly, that large LSB candidates with $r_{50} \geq 3$ kpc seem to be very rare in both cluster cores.

5.3 Uncertainties

In Fig. 6 we try to include realistic photometric uncertainties for our sample. Our major source of uncertainty in the measured total fluxes, which translate to uncertainties in half light radii and surface brightnesses, lies in the adopted background level (see Section 4). To test how large the resulting uncertainties are, we probed this using in-
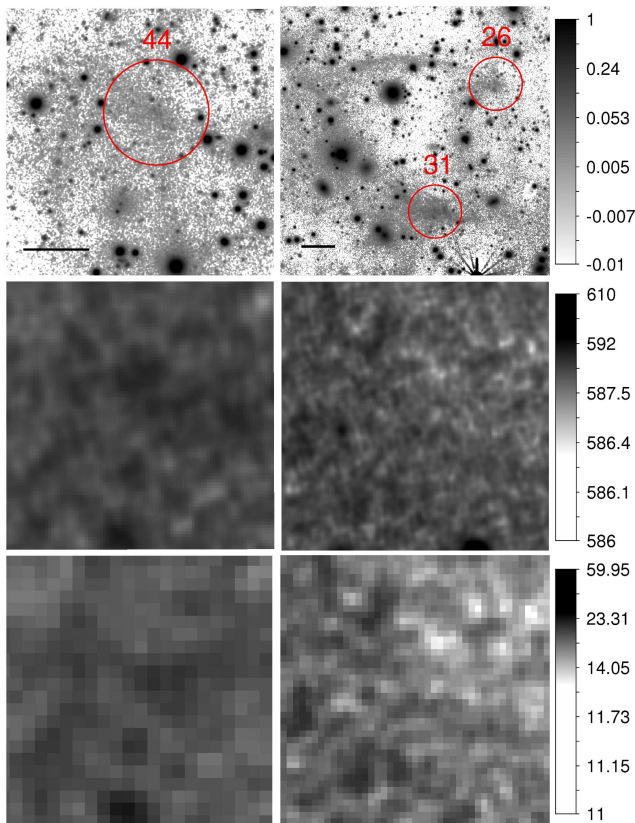
Figure 7. Objects from our sample that could be either LSB galaxies with possible tidal streams or cirrus emission. The top panels show the objects in our smoothed data, marked with red circles. The four lower panels show the corresponding regions in the WISE 12μm intensity maps that trace Galactic cirrus. The original WISE intensity maps with 6 arcsec resolution are displayed in the middle panels, the reprocessed WISE intensity maps with 15 arcsec resolution that were cleaned from point sources are shown in the bottom panels. The height and width of the cutout regions is 2 arcmin ($\hat{=}$ 41 kpc) in the left panels and 4 arcmin ($\hat{=}$ 81 kpc) in the right panels, respectively. The black bar in the images in the top panels denotes a length of 10 kpc. We see no obvious correspondence between the structures observed in our data and the 12μm emission. We therefore cannot draw any firm conclusions on the nature of these structures.

serted LSB galaxy models that were generated similarly to those described in Section 3. We created eight model types that span the parameter range of our sample. Four model types have $\langle\mu_V\rangle_{50} = 25.5$ mag arcsec^{-2}, the other four have $\langle\mu_V\rangle_{50} = 26.5$ mag arcsec^{-2}, with varying magnitudes $M_V = -12.5$ to -15.5 mag and sizes $0.8 \leq r_{50} \leq 4.9$ kpc. The models have one component Sérsic profiles with n=1, are nearly round (ellipticity = 0.1) and were convolved to our average seeing FWHM. We inserted ten models of each type into one copy of our mosaic, respectively. We then measured M_V, r_{50} and $\langle\mu_V\rangle_{50}$ similarly to our sample of real LSB candidates. We calculated the average offset between true and measured parameters for each model type, as well as the scatter of the measured parameters.

We indicate the average parameter offsets with arrows in the right panels of Fig. 6. The arrow tips point to the true values, with M_V being systematically estimated as too faint by on average 0.4 mag, and r_{50} being underestimated

by on average 0.5 kpc. We largely preserved the true surface brightness, which results from our approach of considering the uncontaminated part of the flux profile only (see Section 4). The offsets in $\langle\mu_V\rangle_{50}$ are small, and do not exceed 0.1 mag arcsec^{-2}. In general the parameter offsets are more severe for model types with the largest size and faintest surface brightness, and negligible for model types with the smallest size and brightest surface brightness. The error bars in Fig. 6 give the standard deviation of the measured M_V, r_{50} and $\langle\mu_V\rangle_{50}$ values for each model type, with average standard deviations of $\Delta M_V = \pm 0.3$ mag, $\Delta r_{50} = \pm 0.3$ kpc and $\langle\mu_V\rangle_{50} = \pm 0.1$ mag arcsec^{-2}.

We also tested the implications of our estimated uncertainties on our results from Section 5.2, and applied the average systematic offsets in M_V, r_{50} and $\langle\mu_V\rangle_{50}$ between the models and the measured parameters of our LSB galaxy sample. In this case the number of LSB candidates in the considered parameter range of $M_V \leq -14$ mag and $r_{50} \geq 2$ kpc would increase to 25 candidates in the Perseus cluster core, but still only two LSB candidates would have sizes larger than $r_{50} \geq 3$ kpc. Thus, while the number of LSB candidates would now be significantly higher in Perseus compared to the number of LSB candidates in the same parameter range in the Coma cluster core, the conclusion of only finding very few large LSB galaxy candidates in the cluster core would remain unchanged.

Since the core regions of massive clusters are characterized by a particularly high density of galaxies, one possible concern is that this may have influenced our ability of detecting large LSB galaxy candidates with $r_{50} \geq 3$ kpc. Our tests with the inserted LSB galaxy models indicate, however, that we are in principle able to detect objects with $r_{50} > 3$ kpc in the surface brightness range $\langle\mu_V\rangle_{50} < 27$ mag arcsec^{-2} in our data, if these were present (see Section 3). Nevertheless we might have missed objects in close vicinity to bright cluster galaxies or foreground stars, although we modelled and subtracted the light profile of the latter in most cases. The apparent absence of LSB candidates in regions around bright sources in Fig. 4 might therefore not be a real effect.

Due to the location of the Perseus cluster at low Galactic latitude ($l = 13°$) we cannot exclude the presence of diffuse emission from Galactic cirrus in our data. Cirrus is often visible in deep wide-field imaging data, and the resulting structures can be very similar in appearance to stellar tidal streams (cf. Miville-Deschênes et al. 2016). We therefore compared our candidates with possible streams to the WISE[12] 12μm data that trace Galactic cirrus, in order to search for possible counterparts in the 12μm emission. Fig. 7 shows our data in comparison to both the original WISE data with 6 arcsec resolution, as well as to the reprocessed data from Meisner & Finkbeiner (2014) with 15 arcsec resolution that were cleaned from point sources. We clearly see diffuse emission in the 12μm data at the position of Perseus. However, we are not able to identify obvious structures in the WISE maps that would match to the candidates with possible streams we observe in our data, due to the insufficient resolution of the latter. Therefore we neither can confirm

---

[12] Wide-field Infrared Survey Explorer (Wright et al. 2010)

nor exclude that the nature of these structures may be cirrus emission rather than LSB galaxy candidates with tidal streams.

6 DISCUSSION

We detected a large number of 89 faint LSB galaxy candidates with $\langle \mu_V \rangle_{50} \geq 24.8\,\mathrm{mag\,arcsec^{-2}}$ in the Perseus cluster core. It is interesting to note that all but one candidate have $r_{50} < 3\,\mathrm{kpc}$. We thus speculate that LSB galaxies with larger sizes cannot survive the strong tidal forces in the core region and possibly have lost already a considerable amount of their dark matter content. This observation is consistent with the study of van der Burg et al. (2016) who found a decreasing number density of faint LSB galaxy candidates in the cores of galaxy clusters. Also the numerical simulations of Yozin & Bekki (2015) predicted the disruption of LSB galaxies orbiting close to the cluster centre.

The effect of tides on LSB galaxies in galaxy clusters is possibly also reflected in the radial number density distribution we observe for our sample. The nearly constant projected number density for cluster-centric distances $r \geq 100\,\mathrm{kpc}$ implies that the three-dimensional distribution should actually increase with distance from the cluster centre. This may be a further argument that LSB galaxies are depleted in the cluster core region due to tidal disruption. Very close to the cluster centre, for cluster-centric distances $r < 100\,\mathrm{kpc}$, the number density drops, with only two LSB candidates from our sample being located in this region. Here tidal effects from the central cluster galaxy NGC 1275 may become apparent (cf. Mathews et al. 2006, fig. 1). For example, the slightly more compact peculiar galaxy SA 0426-002 ($M_B = -16.3\,\mathrm{mag}$, $r_{50} = 2.1\,\mathrm{kpc}$), being located only $\sim 30\,\mathrm{kpc}$ from the cluster centre, shows signs of being tidally disturbed (see Fig. 4, top left panel). Also in the Fornax cluster core a drop in the number density profile of faint LSB candidates is seen within 180 kpc of the cluster centre (Venhola et al. 2017).

We can use the observed limit in r_{50} as a rough constraint on the dark matter content of the LSB candidates in the cluster centre (cf. Penny et al. 2009). The tidal radius R_{tidal} is given by

$$R_{\mathrm{tidal}} = R_{\mathrm{peri}} \left(\frac{M_{\mathrm{obj}}}{M_{\mathrm{cl}}(R_{\mathrm{peri}})\,(3+e)} \right)^{1/3}, \qquad (1)$$

with the pericentric distance R_{peri}, the total object mass M_{obj}, the cluster mass $M_{\mathrm{cl}}(R_{\mathrm{peri}})$ within R_{peri}, and the eccentricity of the orbit e (King 1962). We find about 50 per cent of our sample (44 objects) at projected cluster-centric distances below 330 kpc. Assuming that this is representative of the orbital pericentre for at least a fraction of the population,[13] we estimate R_{tidal} for a typical LSB candidate of our sample with $M_V = -14\,\mathrm{mag}$ and $R_{\mathrm{peri}} = 330\,\mathrm{kpc}$, assuming an eccentric orbit with $e = 0.5$. We adopt the cluster mass profile from Mathews et al. (2006), where $M_{\mathrm{cl}}(330\,\mathrm{kpc}) = 1.3 \times 10^{14}\,\mathrm{M_\odot}$.

Assuming a galaxy without dark matter, and adopting a mass-to-light ratio of $M/L_V = 2$ for an old stellar population with subsolar metallicity (Bruzual & Charlot 2003), the mass of an object with $M_V = -14\,\mathrm{mag}$ would be $M_{\mathrm{obj}} = 7 \times 10^7\,\mathrm{M_\odot}$ accordingly, resulting in a tidal radius of 1.8 kpc. This compares to a range of observed $r_{50} \simeq 1.0 - 2.5\,\mathrm{kpc}$ for LSB candidates from our sample with $M_V \simeq -14\,\mathrm{mag}$. We note that we can generally probe our objects out to more than one half light radius in our data, thus the tidal radius would be within the observed stellar extent. However, since most objects from our sample do not show obvious signs of current disruption, we suspect that they may contain additional mass in order to prevent tidal disruption.

If we assume a higher mass-to-light ratio of $M/L_V = 10$, the tidal radius of the same object would increase to 2.9 kpc. For $M/L_V = 100$ the tidal radius would be $R_{\mathrm{tidal}} = 6.2\,\mathrm{kpc}$, and for $M/L_V = 1000$ we derive $R_{\mathrm{tidal}} = 13.3\,\mathrm{kpc}$. For M/L_V close to 1000 the tidal radius is significantly larger than the observed range of half-light radii. If such a high mass-to-light ratio would be reached within the tidal radius, we might expect to find a higher number of galaxies with $r_{50} \gtrsim 3\,\mathrm{kpc}$ in the cluster core. However, *for $M/L_V \lesssim 100$, the tidal radius would be on the order of 1-2 r_{50}*, which is also consistent with the mass-to-light ratios derived from dynamical measurements of similar galaxies. For example, van Dokkum et al. (2016) found a mass-to-light ratio of ~ 50 within one half-light radius for one LSB galaxy in the Coma cluster ($M_V = -16.1\,\mathrm{mag}$, $r_{50} = 4.3\,\mathrm{kpc}$),[14] and Beasley et al. (2016) derived a mass-to-light ratio of ~ 100 within one half-light radius for one LSB galaxy in Virgo ($M_g = -13.3\,\mathrm{mag}$, $r_{50} = 2.8\,\mathrm{kpc}$).[15] We note that based on similar analytical arguments as described above van Dokkum et al. (2015a) also estimated a dark matter fraction of $\gtrsim 100\,\mathrm{per\,cent}$ within an assumed tidal radius of 6 kpc for a sample of faint LSB candidates within the core region of the Coma cluster.

While the above approach gives an estimate of the radius beyond which material is likely going to be stripped, another approach to estimate the effect of tides on galaxies in clusters is to compare the density of the tidal field to the density of the orbiting galaxy (cf. Gnedin 2003). The density of the tidal field ρ_{tidal} is given by Poisson's equation, $\rho_{\mathrm{tidal}} = F_{\mathrm{tidal}}/(4\pi G)$, where F_{tidal} is the trace of the tidal tensor. We consider the extended mass distribution of the cluster[16] and approximate the strength of the tidal force at a given cluster-centric distance r_0 as $F_{\mathrm{tidal}} = |dg(r)/dr|_{r_0}$, where $g(r)$ is the gravitational acceleration exerted by the mass of the cluster. For $g(r)$ we adopt the gravitational acceleration due to the Perseus cluster potential given by Mathews et al. (2006), where we only consider the contribution of the NFW-profile, which is the dominant component at cluster-centric distances $r \gtrsim 10\,\mathrm{kpc}$. We approximate the average density of the orbiting galaxy, assuming spherical symmetry, as $\rho_{\mathrm{gal}} = M_{\mathrm{gal}}(R)/(4\pi R^3/3)$, where $M_{\mathrm{gal}}(R)$ is the total mass of the galaxy within a radius R. Requiring that the density of the galaxy is larger than the tidal density to

---

[13] While on the one hand, most objects are likely to be situated somewhat further away from the centre than the projected value suggests, on the other hand it is also likely that their orbital pericentre is located further inward from their current location.

[14] Based on stellar dynamics of the galaxy.

[15] Based on GC system dynamics of the galaxy.

[16] Unlike in the first approach, where a point-mass approximation was used.

prevent its disruption, the limiting radius R_{lim} is given as

$$R_{lim} \geq \sqrt[3]{\frac{3GM_{gal}(R)}{|dg(r)/dr|_{r_0}}} \qquad (2)$$

Considering again a typical galaxy from our sample, with $M_V = -14$ mag at a cluster-centric distance $r_0 = 330$ kpc, we find $R_{lim} = 0.8$ kpc for $M/L_V = 2$, $R_{lim} = 1.3$ kpc for $M/L_V = 10$, $R_{lim} = 2.8$ kpc for $M/L_V = 100$, and $R_{lim} = 6.1$ kpc for $M/L_V = 1000$. Thus, in comparison to the tidal radius derived with the first approach, the limiting radius obtained with the second approach is a factor of two smaller. If we assume that $M/L_V = 100$ would be characteristic for a considerable fraction of our sample, then the limiting radius would be on the order of only $1\,r_{50}$.

Does this imply that a few of the largest LSB candidates in the Perseus cluster core should be in process of tidal disruption right now? – We do identify three LSB candidates in Perseus that show possible signs of disruption (see panels on the right hand side in Fig. 4). Candidate 44 appears to be embedded in stream like filaments. It is, however, unclear whether we see here still a bound galaxy or rather a remnant core of a stream. Candidates 26 and 31 seem to be connected via an arc-like tidal stream. This could point to a low-velocity interaction between those two candidates, since such interactions produce the most severe mass loss. The convex shape of the stream with respect to the cluster centre might suggest that these two objects are not in orbit around the cluster centre, but instead still bound to a possibly recently accreted subgroup of galaxies. The association with a subgroup could be supported by the observation that these three candidates, together with the candidate of brighter surface brightness with tidal tails (see Fig. 4, lower left panel), are located closely together in a region southwest of the cluster centre, within a cluster-centric distance range of $300 - 400$ kpc. It is also interesting to note that Merritt et al. (2016) found a generally more complex and distorted morphology for LSB candidates in galaxy groups than in galaxy clusters, indicating that the group environment may play an important role in shaping galaxies of low stellar density.

The comparison to the LSB galaxy samples in Coma (van Dokkum et al. 2015a; Yagi et al. 2016) showed that both cluster cores hold a similar number of faint LSB candidates with $r_{50} \geq 2$ kpc and $M_V \leq -14$ mag. Based on the 1.5 times lower cluster mass of Perseus[17], we would expect a somewhat lower number of all galaxy types in Perseus. However, with regard to the density in the cluster core, both clusters reach a comparable galaxy surface number density within 0.5 Mpc (Weinmann et al. 2011), thus causing comparable disruptive forces in both cluster cores. Therefore, according to the cluster mass and density, we would expect a similar or even lower number of LSB galaxies of such large size in Perseus, which is in agreement with our observations.

One important question to investigate would be whether there exists a possible evolutionary link between LSB galaxies that are red and quiescent and those that are blue and star-forming. The cosmological simulations of

Di Cintio et al. (2017) suggest that faint LSB galaxies with large sizes may form as initially gas-rich starforming systems in low density environments. In this context, the quenching of star formation should be related to external processes, like, e.g., ram pressure stripping. Román & Trujillo (2016) examined a sample of faint LSB candidates in group environments. Since they found the red LSB candidates closer to the respective group's centre than the blue systems this could imply that the group environment was efficient in removing the gas that fuels star formation. This is also seen among the dwarf galaxies of the Local Group, which show a pronounced morphology - gas content - distance relation (see Grebel et al. 2003). However a few quiescent and gas-poor LSB galaxies of dwarf luminosity are also observed in isolation (e.g. Papastergis et al. 2017), which would not fit into this scenario. An essential aspect would be to understand whether the physical processes governing the formation and evolution of LSB galaxies are controlled by stellar density or by stellar mass. The latter could possibly explain the observed wide variety of LSB galaxy properties from low-mass dSphs to massive LSB disk galaxies.

7 SUMMARY AND CONCLUSIONS

We obtained deep V-band imaging data under good seeing conditions of the central regions of Perseus with PFIP at the WHT that we used to search for faint LSB galaxies in the surface brightness range of the so-called 'ultra-diffuse galaxies'. We detected an abundant population of 89 faint LSB galaxy candidates for which we performed photometry and derived basic structural parameters. Our sample is characterized by mean effective surface brightnesses $24.8 \leq \langle \mu_V \rangle_{50} \leq 27.1$ mag arcsec^{-2}, total magnitudes $-11.8 \geq M_V \geq -15.5$ mag and half-light radii $0.7 \leq r_{50} \leq 4.1$ kpc. A comparison to overlapping HST/ACS imaging data indicates that the sample is relatively uncontaminated by background objects.

We find good evidence for tidal disruption leading to a deficiency of LSB galaxy candidates in the central regions of the cluster. This is indicated by a constant observed number density beyond cluster-centric distances of 100 kpc and the lack of very large LSB candidates with $r_{50} \geq 3$ kpc except for one object. However, only a few candidates show structural evidence of ongoing tidal disruption. If LSB systems are to remain gravitationally bound in the cluster core, the density limits set by the Perseus cluster tidal field require that they have high M/L values of about 100, assuming a standard model for gravity.

In comparison to the Coma cluster – with its comparable central density to Perseus – we find that our sample statistically resembles the LSB galaxy population in the central regions of Coma. Given the same dearth of large objects with $r_{50} \geq 3$ kpc in both cluster cores we conclude that these cannot survive the strong tides in the centres of massive clusters.

---

[17] Assuming $M_{vir,Coma} = 1.3 \times 10^{15}$ $M_\odot$ (Łokas & Mamon 2003) and $M_{vir,Perseus} = 8.5 \times 10^{14}$ $M_\odot$ (Mathews et al. 2006).

ACKNOWLEDGEMENTS

REFERENCES

Adami C., et al., 2006, A&A, 459, 679
Ahn C. P., et al., 2012, ApJS, 203, 21
Andreon S., 1994, A&A, 284, 801
Beasley M. A., Trujillo I., 2016, ApJ, 830, 23
Beasley M. A., Romanowsky A. J., Pota V., Navarro I. M., Martinez Delgado D., Neyer F., Deich A. L., 2016, ApJ, 819, L20
Bertin E., Arnouts S., 1996, A&AS, 117, 393
Binggeli B., Sandage A., Tammann G. A., 1985, AJ, 90, 1681
Boissier S., et al., 2016, A&A, 593, A126
Bothun G. D., Impey C. D., Malin D. F., 1991, ApJ, 376, 404
Bruzual G., Charlot S., 2003, MNRAS, 344, 1000
Conselice C. J., Gallagher III J. S., Wyse R. F. G., 2002, AJ, 123, 2246
Conselice C. J., Gallagher III J. S., Wyse R. F. G., 2003, AJ, 125, 66
Dalcanton J. J., Spergel D. N., Gunn J. E., Schmidt M., Schneider D. P., 1997, AJ, 114, 635
Di Cintio A., Brook C. B., Dutton A. A., Macciò A. V., Obreja A., Dekel A., 2017, MNRAS, 466, L1
Dunn J. M., 2010, MNRAS, 408, 392
Erben T., et al., 2005, Astronomische Nachrichten, 326, 432
Ferguson H. C., Sandage A., 1988, AJ, 96, 1520
Ferrarese L., et al., 2016, ApJ, 824, 10
Forman W., Jones C., 1982, ARA&A, 20, 547
Gnedin O. Y., 2003, ApJ, 589, 752
Graham A. W., Driver S. P., 2005, Publ. Astron. Soc. Australia, 22, 118
Grebel E. K., Gallagher III J. S., Harbeck D., 2003, AJ, 125, 1926
Impey C., Bothun G., Malin D., 1988, ApJ, 330, 634
Impey C. D., Sprayberry D., Irwin M. J., Bothun G. D., 1996, ApJS, 105, 209
Jester S., et al., 2005, AJ, 130, 873
Joye W. A., Mandel E., 2003, in Payne H. E., Jedrzejewski R. I., Hook R. N., eds, Astronomical Society of the Pacific Conference Series Vol. 295, Astronomical Data Analysis Software and Systems XII. p. 489
Kadowaki J., Zaritsky D., Donnerstein R. L., 2017, preprint, (arXiv:1703.02042)
King I., 1962, AJ, 67, 471
Kniazev A. Y., Grebel E. K., Pustilnik S. A., Pramskij A. G., Kniazeva T. F., Prada F., Harbeck D., 2004, AJ, 127, 704
Koch A., Burkert A., Rich R. M., Collins M. L. M., Black C. S., Hilker M., Benson A. J., 2012, ApJ, 755, L13
Koda J., Yagi M., Yamanoi H., Komiyama Y., 2015, ApJ, 807, L2
Lieder S., Lisker T., Hilker M., Misgeld I., Durrell P., 2012, A&A, 538, A69
Lisker T., Weinmann S. M., Janz J., Meyer H. T., 2013, MNRAS, 432, 1162
Lisker T., Wittmann C., Pasquali A., Hilker M., Grebel E. K., 2017, (submitted to A&A)
Łokas E. L., Mamon G. A., 2003, MNRAS, 343, 401
Mathews W. G., Faltenbacher A., Brighenti F., 2006, ApJ, 638, 659
McConnachie A. W., 2012, AJ, 144, 4
Meisner A. M., Finkbeiner D. P., 2014, ApJ, 781, 5
Merritt A., van Dokkum P., Danieli S., Abraham R., Zhang J., Karachentsev I. D., Makarova L. N., 2016, ApJ, 833, 168
Mihos J. C., et al., 2015, ApJ, 809, L21
Mihos J. C., Harding P., Feldmeier J. J., Rudick C., Janowiecki S., Morrison H., Slater C., Watkins A., 2017, ApJ, 834, 16
Milgrom M., 2015, MNRAS, 454, 3810
Miville-Deschênes M.-A., Duc P.-A., Marleau F., Cuillandre J.-C., Didelon P., Gwyn S., Karabal E., 2016, A&A, 593, A4
Muñoz R. P., et al., 2015, ApJ, 813, L15
Papastergis E., Adams E. A. K., Romanowsky A. J., 2017, preprint, (arXiv:1703.05610)
Peng E. W., Lim S., 2016, ApJ, 822, L31
Penny S. J., Conselice C. J., de Rijcke S., Held E. V., 2009, MNRAS, 393, 1054
Penny S. J., Forbes D. A., Pimbblet K. A., Floyd D. J. E., 2014, MNRAS, 443, 3381
Piffaretti R., Arnaud M., Pratt G. W., Pointecouteau E., Melin J.-B., 2011, A&A, 534, A109
Román J., Trujillo I., 2016, preprint, (arXiv:1610.08980)
Sandage A., Binggeli B., 1984, AJ, 89, 919
Schirmer M., 2013, ApJS, 209, 21
Schlafly E. F., Finkbeiner D. P., 2011, ApJ, 737, 103
Schombert J., Maciel T., McGaugh S., 2011, Advances in Astronomy, 2011, 143698
Simionescu A., et al., 2011, Science, 331, 1576
Sprayberry D., Impey C. D., Bothun G. D., Irwin M. J., 1995, AJ, 109, 558
Struble M. F., Rood H. J., 1999, ApJS, 125, 35
Venhola A., et al., 2017, (submitted to A&A)
Weinmann S. M., Lisker T., Guo Q., Meyer H. T., Janz J., 2011, MNRAS, 416, 1197
Wright E. L., et al., 2010, AJ, 140, 1868
Yagi M., Koda J., Komiyama Y., Yamanoi H., 2016, ApJS, 225, 11
Yozin C., Bekki K., 2015, MNRAS, 452, 937
de Blok W. J. G., McGaugh S. S., van der Hulst J. M., 1996, MNRAS, 283, 18
de Rijcke S., Penny S. J., Conselice C. J., Valcke S., Held E. V., 2009, MNRAS, 393, 798
van Dokkum P. G., Abraham R., Merritt A., Zhang J., Geha M., Conroy C., 2015a, ApJ, 798, L45
van Dokkum P. G., et al., 2015b, ApJ, 804, L26
van Dokkum P., et al., 2016, ApJ, 828, L6
van den Bergh S., 1959, Publications of the David Dunlap Observatory, 2, 147
van der Burg R. F. J., Muzzin A., Hoekstra H., 2016, A&A, 590, A20